communications physics

A Nature Portfolio journal

Article

https://doi.org/10.1038/s42005-025-02174-2

Pressure tuning of Kitaev spin liquid candidate $Na_3Co_2SbO_6$

Check for updates

E. H. T. Poldi[1,2], R. Tartaglia[2,3], G. Fabbris[2], N. Nguyen[1], H. Park[1,4], Z. Liu[1], M. van Veenendaal[2,5], R. Kumar[1], G. Jose[6], S. Samanta[6], W. Bi[6], Y. Xiao[7], D. Popov[7], Y. Wu[8], J.-W. Kim[2], H. Zheng[4], J. Yan[9], J. F. Mitchell[4], R. J. Hemley[10] & D. Haskel[2] ✉

The search for Kitaev's quantum spin liquid in real materials has recently expanded with the prediction that honeycomb lattices of divalent, high-spin cobalt ions could host the dominant bond-dependent exchange interactions required to stabilize the elusive entangled quantum state. The layered honeycomb $Na_3Co_2SbO_6$ has been singled out as a leading candidate provided that the trigonal crystal field acting on Co 3*d* orbitals, which enhances non-Kitaev exchange interactions between $J_{\mathrm{eff}} = \frac{1}{2}$ spin-orbital pseudospins, is reduced. Here we show that applied pressure leads to anisotropic compression of the layered structure, significantly reducing the trigonal distortion of CoO_6 octahedra. Ferromagnetic correlations between pseudospins are enhanced in the spin-polarized (3 Tesla) phase up to about 60 GPa. Higher pressures drive a high-spin to low-spin transition destroying the $J_{\mathrm{eff}} = \frac{1}{2}$ moments required to map the spin Hamiltonian into Kitaev's model. The spin transition strongly suppresses the low-temperature magnetic susceptibility and appears to stabilize a paramagnetic phase driven by frustration. The possible emergence of frustrated magnetism of localized $S = \frac{1}{2}$ moments opens the door for exploration of novel magnetic quantum states in compressed honeycomb lattices of divalent cobaltates.

The quest to realize Kitaev's theoretical quantum spin liquid (KQSL) state in real materials is partly driven by the prediction that a magnetic field would drive the gapless solution of Kitaev's model into a gapped phase with anyonic excitations amenable to topologically protected quantum computing[1–4]. The materials search has up to recently been largely focused on honeycomb lattices of Ru^{3+} and Ir^{4+} transition metal (TM) ions with a d^5 configuration, where a large octahedral crystal field rooted in extended 4*d*/5*d* orbitals stabilizes a low-spin $t_{2g}^5 e_g^0$ state and where strong spin-orbit coupling entangles orbital $l_{\mathrm{eff}} = 1$ and spin $s = \frac{1}{2}$ moments into $j_{\mathrm{eff}} = \frac{1}{2}$ pseudospins[5]. The spin-orbital entanglement introduces bond-directional exchange anisotropy, which in perfect honeycomb lattices of edge-shared octahedra, maps the 90-degree TM-O-TM superexchange interactions into Kitaev's model[6]. Although sizable Kitaev exchange (*K*) interactions are found in a number of two-dimensional 4*d* and 5*d* honeycomb lattices, including the heavily studied $RuCl_3$, A_2IrO_3 (A = Na, Li), and $A_3LiIr_2O_6$ (A = H, Ag)[7], with the exception of $H_3LiIr_2O_6$ all order magnetically as a result of competing isotropic Heisenberg (*J*) and off-diagonal anisotropic (Γ, Γ') exchange interactions. These non-Kitaev superexchange couplings emerge from distortions away from the ideal honeycomb lattice, such as those driven by trigonal distortions of TMO_6 octahedra, which lift the electronic degeneracy of t_{2g} states and modify the spin-orbital pseudospin wavefunction. Other non-Kitaev interactions include direct isotropic exchange from $d-d$ overlap between extended 4*d*/5*d*-orbitals.

The more localized nature of 3*d* orbitals makes them attractive for the suppression of direct exchange terms. A smaller octahedral crystal field and larger intra-atomic Hund's coupling relative to the 4*d*/5*d* case stabilizes the high-spin (HS), $t_{2g}^5 e_g^2$ configuration in Co^{2+} ions. Spin-orbit coupling combines the $l_{\mathrm{eff}} = 1$ state formed by the single hole in the 3-fold degenerate t_{2g} states with the total $S = \frac{3}{2}$ spin of t_{2g} and e_g orbitals, leading to a many body $J_{\mathrm{eff}} = \frac{1}{2}$ pseudospin ground state with excited $J_{\mathrm{eff}} = \frac{3}{2}, \frac{5}{2}$ multiplets (we

[1]Department of Physics, University of Illinois at Chicago, Chicago, IL, 60607, USA. [2]Advanced Photon Source, Argonne National Laboratory, Lemont, IL, 60439, USA. [3]Instituto de Física Gleb Wataghin, Universidade Estadual de Campinas (UNICAMP), Campinas, São Paulo, 13083-859, Brazil. [4]Materials Science Division, Argonne National Laboratory, Argonne, IL, 60439, USA. [5]Department of Physics, Northern Illinois University, DeKalb, IL, 60115, USA. [6]Department of Physics, University of Alabama at Birmingham, Birmingham, AL, 35294, USA. [7]HPCAT, Advanced Photon Source, Argonne National Laboratory, Argonne, IL, 60439, USA. [8]Neutron Scattering Division, Oak Ridge National Laboratory, Oak Ridge, TN, 37831, USA. [9]Materials Science and Technology Division, Oak Ridge National Laboratory, Oak Ridge, TN, 37831, USA. [10]Departments of Physics, Chemistry and Earth and Environmental Sciences, University of Illinois at Chicago, Chicago, IL, 60607, USA. ✉e-mail: haskel@anl.gov

use lower-case j for single-particle states and upper-case J for many-body states). However, the order-of-magnitude weaker spin-orbit coupling (tens vs. hundreds of meV) makes for a delicate spin-orbital pseudospin moment, which is fragile against non-cubic crystal fields arising from lattice distortions. Perfect honeycomb lattices of HS Co^{2+} ions have been predicted to host dominant ferromagnetic Kitaev interactions between $J_{\mathrm{eff}} = \frac{1}{2}$ pseudospins, primarily arising from t_{2g}-e_g superexchange pathways[8–10]. Inelastic neutron scattering[11–13] and Co $L_{2,3}$-edge x-ray spectroscopy[14] provided support for a $J_{\mathrm{eff}} = \frac{1}{2}$ description of the ground state in the trigonally distorted honeycomb lattices $Na_2Co_2TeO_6$ and $Na_3Co_2SbO_6$, based on measurements of spin-orbit excitations and orbital-to-spin moment ratios, respectively. Whether Kitaev interactions are dominant in these and the related $BaCo_2(AsO_4)_2$ remains a matter of debate, with both $KJ\Gamma\Gamma'$[11,13] and XXZ easy-plane[15,16] spin Hamiltonians being proposed to explain the zig-zag-like magnetic order and spectrum of low-energy magnetic excitations. However, in analogy to $RuCl_3$ where a ~7 T applied magnetic field suppresses magnetic order at a quantum critical point giving rise to a gapped continuum of magnetic excitations resembling those of a KQSL[17,18], magnetic fields below 2 T suppress the antiferromagnetic, zig-zag-like double-Q[15,19,20] magnetic structure of $Na_3Co_2SbO_6$ leading to a quantum critical regime featuring a magnetically disordered, spin-liquid-like phase before a spin-polarized phase with gapped magnetic excitations emerges at higher fields[21–23]. The much-reduced critical fields needed to enter a quantum critical regime in $Na_3Co_2SbO_6$ and $BaCo_2(AsO_4)_2$[24] relative to $RuCl_3$ suggest weaker non-Kitaev interactions.

Here we explore whether pressure can stabilize a KQSL state. We focus on $Na_3Co_2SbO_6$, which is predicted to host a KQSL state if the trigonal crystal field can be at least halved[8,9]. Applied pressure allows for continuous tuning of interatomic distances, bond angles, and degree of covalency in TM-O bonds, which dictate crystal fields and exchange interactions. The localized nature of $3d$ orbitals renders cobaltates much more robust against dimerization and formation of molecular orbitals between closely spaced TM ions across edge-shared octahedra. Such pressure-induced dimerization is prevalent in $4d/5d$ honeycomb lattices[25–30] and leads to the collapse of their spin-orbital $j_{\mathrm{eff}} = \frac{1}{2}$ moments required to stabilize the KQSL state[31]. On the other hand, the weak spin-orbit coupling and proclivity of HS Co^{2+} ions to undergo spin transitions under increasing octahedral crystal field may render the many-body $J_{\mathrm{eff}} = \frac{1}{2}$ moment unstable against lattice compression. We find that quasi-hydrostatic pressure leads to anisotropic lattice compression, which, based on density functional theory calculations of relaxed atomic positions, results in a continuous, sizable reduction of the trigonal distortion in CoO_6 octahedra. A significant enhancement of ferromagnetic correlations between pseudospins is observed in the spin-polarized phase ($H = 3$ T) below about 60 GPa. While Kitaev exchange interactions in HS $3d^7$ cobaltates are always ferromagnetic[8–10], magnetization near full moment values in 3 T applied field that persists to rather high temperatures points to enhanced Heisenberg ferromagnetic interactions between pseudospins. Pressures above about 70 GPa lead to a spin transition to a low-spin (LS) Co $3d^7$ state, quenching the orbital degrees of freedom at the root of bond-directional Kitaev's exchange. While pressure does not stabilize a KQSL state, the honeycomb arrangement of LS Co^{2+} ions shows a vanishing low-temperature magnetic susceptibility at 100 GPa, suggestive of a paramagnetic ground state driven by frustration, as predicted by $J_1 - J_2 - J_3$ quantum models of honeycomb lattices[32,33]. Since the LS Co $3d^7$ configuration is rarely found at ambient conditions, the results highlight the potential of high-pressure studies to unravel novel frustrated magnetic states in cobaltate honeycomb lattices.

Results

Crystal structure and trigonal distortion

X-ray powder diffraction data were collected as a function of pressure at selected temperatures in the 8 K to 300 K range. Full data sets and corresponding Le Bail fits are shown in Supplementary Figs. S1 and S2. An expanded view (log scale) of 0.5 GPa and 70 GPa data is shown in Fig. 1a. Le Bail fits using the known monoclinic structure at ambient pressure[19] provide a good description of the data over the entire pressure range. No new Bragg peaks are observed, indicating the absence of structural phase transitions, including dimerization.

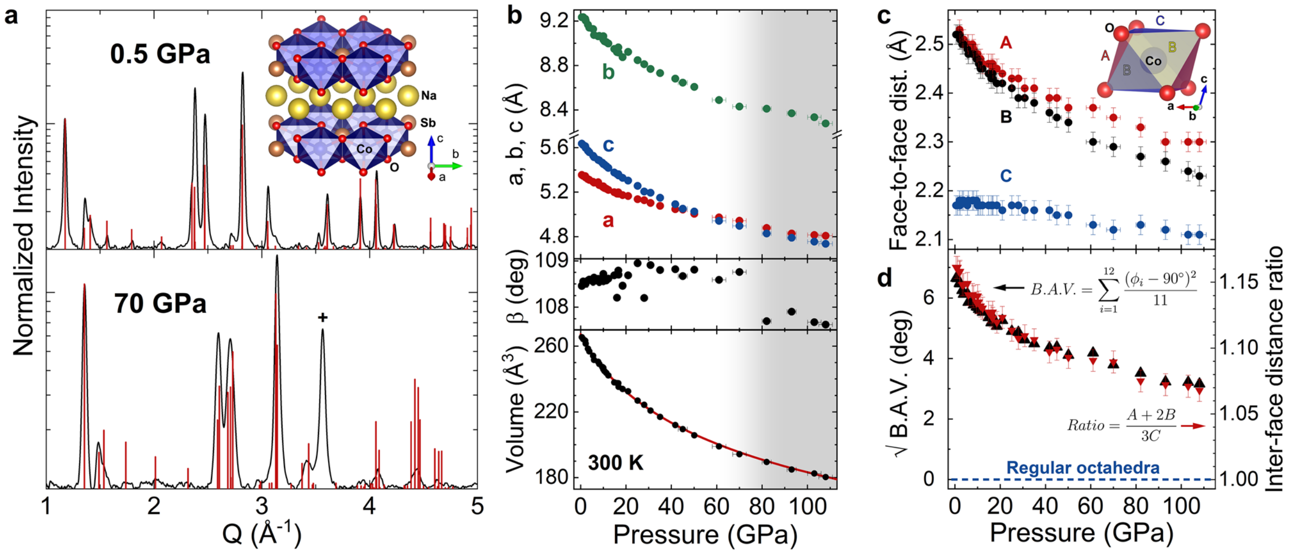

Fig. 1 | Evolution of crystal structure and trigonal distortion probed with x-ray diffraction. a Diffraction patterns at 0.5 and 70 GPa at room temperature, shown in log scale to enhance low intensity peaks. Symbol + denotes a Bragg peak from the neon pressure transmitting medium. Red bars represent theoretically calculated Bragg peak positions (VESTA[82]) using the ambient pressure space group and atomic positions[19] and experimental lattice parameters. Intensities are normalized to the most intense Bragg peak at ~2.8 Å^{-1}. Crystal structure viewed along the a-axis is shown in the inset. **b** Monoclinic lattice parameters a, b, c and β and unit cell volume V (points) alongside fitted third-order Birch-Murnaghan equation of state (line). The shaded region above 70 GPa features lattice anomalies as a result of a spin transition. Error bars in lattice parameters and derived volume, smaller than symbol size, are those obtained from Le Bail fitting. **c** Distances between O_3 facets in CoO_6 octahedra obtained from density functional theory plus Hubbard U (DFT+U) calculations of relaxed atomic positions using experimental lattice parameters. Inset shows CoO_6 octahedron with pairs of facets labeled A, B, and C, with monoclinic lattice vectors for reference. Errors in O_3 facet distances account for opposite facets not being exactly parallel. **d** Evolution of trigonal distortion with pressure quantified using bond angle variance and asymmetry in O_3 facet distances. Pressure error bars are estimated from pressure gradients over the illuminated sample volume.

Figure 1b shows the pressure dependence of lattice parameters. The pressure-volume relation, also shown in Fig. 1b can be fitted by a single equation of state using either a 3rd-order Birch-Murnaghan model[34] or Vinet model[35,36]. The smooth P–V relation is also indicative of the absence of structural phase transitions. Both models yield consistent ambient pressure-volume values of $V_0 = 266.2 \pm 0.3$ Å^3. Fitted values for bulk modulus and its pressure derivative at 1 atm are $B_0 = 99 \pm 3$ (97 ± 3) GPa and $B_0' = 5.2 \pm 0.2$ (5.5 ± 0.2) using the Birch-Murnaghan (Vinet) models, respectively. Despite the apparent absence of structural transitions, anomalies are observed in structural parameters above about 70 GPa, as evidenced in the non-monotonic response of the b-axis and the monoclinic β angle. As discussed below, a transition from HS to LS Co^{2+} states is detected in the 60–70 GPa pressure range. The smaller atomic volume[37], coupled with Jahn-Teller activity of LS divalent Co ions, is expected to manifest lattice anomalies. We note that Bragg peak broadening at the highest pressures and the limited number of Bragg peaks accessible within the angular aperture of the diamond anvil cell (DAC) hinders detection of small peak splittings that would signal a lowering of symmetry, were it to take place. Forcing the monoclinic β angle to its low-pressure value results in a small volume drop of ~1.6% around 70 GPa, albeit with a significantly worse fit quality (see Supplementary Note 1 and Fig. S3). For comparison, $PbCoO_3$ shows no volume discontinuity at its HS to LS transition centered around 10 GPa[38]. CoO shows a 2.7% volume change across a 90 GPa transition between rhombohedral phases with different densities, presumably connected with a spin transition[39], although XES shows the spin transition taking place at 140 GPa and only after laser heating[40].

Poor powder averaging as a result of the limited sample volume in the DAC, together with weak X-ray scattering power for low-Z oxygen ions, prevented reliable Rietveld refinement of atomic positions. High-pressure single-crystal X-ray diffraction and neutron powder diffraction experiments were attempted. The presence of stacking faults and twin domains in our single crystals made it extremely challenging to reach a structural solution. A high background in neutron powder diffraction resulted in very few observable Bragg peaks, preventing Rietveld refinements. Therefore, pressure-dependent experimental lattice parameters from Le Bail fits were used in density functional theory plus Hubbard U (DFT + U) calculations of relaxed atomic positions to obtain the evolution of trigonal distortion with pressure. Figure 1c shows the distances between pairs of opposite O_3 facets in the distorted CoO_6 octahedra. Figure 1d quantifies the bond angle variance (BAV) of their twelve O-Co-O angles[41] alongside a normalized difference between in-plane and out-of-plane O_3 facet distances. At ambient pressure, CoO_6 octahedra are compressed along their trigonal axis, which is normal to the ab honeycomb planes (close, but not aligned with, monoclinic c-axis). They become more regular under compression as the distances between A-A and B-B facets shrink faster than that between C-C-facets, also leading to a reduction in BAV (regular octahedra have BAV = 0). Noteworthy, the C-facets with surface normal oriented close to the c-axis are less affected by the anisotropic lattice compression of the layered structure (higher along c-axis) up to about 50 GPa, likely due to the ability of the spacer sodium layer between Co-Sb honeycomb layers to accommodate much of the c-axis compression up to this pressure. The trigonal distortion decreases continuously upon compression, roughly reaching half its ambient pressure value at the highest pressures.

Magnetism and local moments

The evolution of magnetism with pressure was probed with x-ray magnetic circular dichroism (XMCD) measurements at the Co K-edge on a powder sample. Figure 2b shows the isotropic x-ray absorption near edge structure (XANES) spectra obtained by averaging over x-ray helicity, while Fig. 2c, d show circular dichroic spectra. Measurements below 10 GPa were done at $T = 2$ K, while measurements above this pressure were done at 4 K to prevent freezing of the pressurized He gas in compression and decompression membranes that actuate on the DAC piston for in-situ pressure control. A 3 T field was applied to probe the evolution of magnetism within the in-field polarized phase. A weak pre-edge feature at 7.708 keV probes Co 3d states via quadrupolar $1s \rightarrow 3d$ excitation, while higher energy features, including the main "white line" peak at ~7.726 keV, correspond to dipolar $1s \rightarrow 4p$ excitations. At ambient pressure, circular dichroic signals have peak intensity values of 0.2% and 1% at pre-edge and white line positions, respectively (see Supplementary Fig. S6). The quadrupolar pre-edge feature remains constant in energy upon compression, and so does the "on-edge" dipolar shoulder feature (some fine structure appearing on this on-edge feature in some of the spectra is an artifact of Bragg diffraction from diamond anvils, noted with * symbols).

The main white line peak and its related dichroic signal gradually shift to higher energy up to about 60–70 GPa, for an overall shift of ~1.8 eV (see Supplementary Fig. S5). The increased separation between the white line and "on-edge" features results in the observable splitting of the dipolar dichroic signal. We attribute these energy shifts to increases in the crystal field and/or hybridization involving the more extended Co 4p states. The energy shifts appear to slow down above 60–70 GPa relative to expectation from volume contraction (see Supplementary Fig. S5). As discussed below, a spin transition is observed in this pressure range.

The rather similar line shape of the isotropic spectra over the entire pressure range is consistent with the absence of structural transitions, in line with results from XRD (the increase in amplitude of the high-energy feature is due to stiffening of the lattice). The evolution of the integrated intensity of the dipolar and quadrupolar dichroic signals is shown in Fig. 2e. Although the dipolar signal does not probe 3d magnetism directly, it is well established that the polarization of 4p states by the 3d–4p interaction enables use of 4p circular dichroism as a proxy of 3d magnetism. This is clearly seen by comparing the temperature and field dependence of conventional magnetometry data (see Supplementary Fig. S4) with that of the integrated intensity of dipolar XMCD signal, both obtained at 1 atm (solid lines and open circles in Fig. 2f, g). While the quadrupolar dichroic pre-edge signal is harder to study systematically due to its smaller size, the evolution of its integrated intensity is in overall agreement with that of the dipolar feature (Fig. 2e).

As seen in Fig. 2e, the magnetization of the in-field ($H = 3$ T) polarized phase measured at 4 K is rather constant up to about 50–60 GPa, then decreases to vanish at about 100 GPa. The XMCD signal can be scaled to sample magnetization using ambient pressure magnetometry data (solid lines in Fig. 2f, g). Temperature-dependent XMCD data collected at $P = 57$ GPa, shown in Fig. 2f (raw data shown in Supplementary Fig. S6), point to enhanced ferromagnetic correlations at this pressure with sizable field-induced magnetization persisting to much higher temperatures than at ambient pressure. Despite the significant ferromagnetic correlation present in the field-induced polarized phase, it does not exhibit spontaneous ferromagnetic order. The enhancement in magnetic correlations can be crudely estimated using a simple Ising model with ferromagnetic nearest-neighbor interactions in the presence of a 3 T applied field, yielding approximate J/k_B values ~15 K and ~ 50 K for 1 atm and 57 GPa, respectively (see Supplementary Note 2 and Fig. S7). Consequently, pressure appears to enhance the ferromagnetic interaction in the field-induced polarized phase, resulting in roughly a three-fold increase in the strength of ferromagnetic exchange at 57 GPa.

Field-dependent XMCD data at $T = 4$ K for pressures above 60 GPa are shown in Fig. 2g (raw data shown in Supplementary Fig. S8). These data demonstrate an enhancement with pressure of the field required to induce polarization, and a strong reduction in saturation magnetization at 6 T. Furthermore, the magnetic susceptibility is progressively suppressed, ultimately vanishing at 100 GPa within the accuracy of our measurements.

To probe the evolution of $J_{\rm eff} = \frac{1}{2}$ pseudospins in Co^{2+} ions, non-resonant Co Kβ x-ray emission spectroscopy (XES) was employed. In the presence of a 3d spin moment, the two final states of 3p to 1s Kβ emission (spin-up or spin-down hole in 3p orbital) are separated in energy by 3p–3d intra-atomic exchange resulting in a primary K$\beta_{1,3}$ line and a Kβ' satellite. The intensity of the satellite is proportional to the 3d spin moment, which also influences the energy separation between the emission lines[42,43]. While a sensitive probe of local moment, XES is insensitive to spin correlations when measured without manipulation or analysis of x-ray polarization[44]. XES data as a function of pressure, collected primarily at 300 K but also at selected

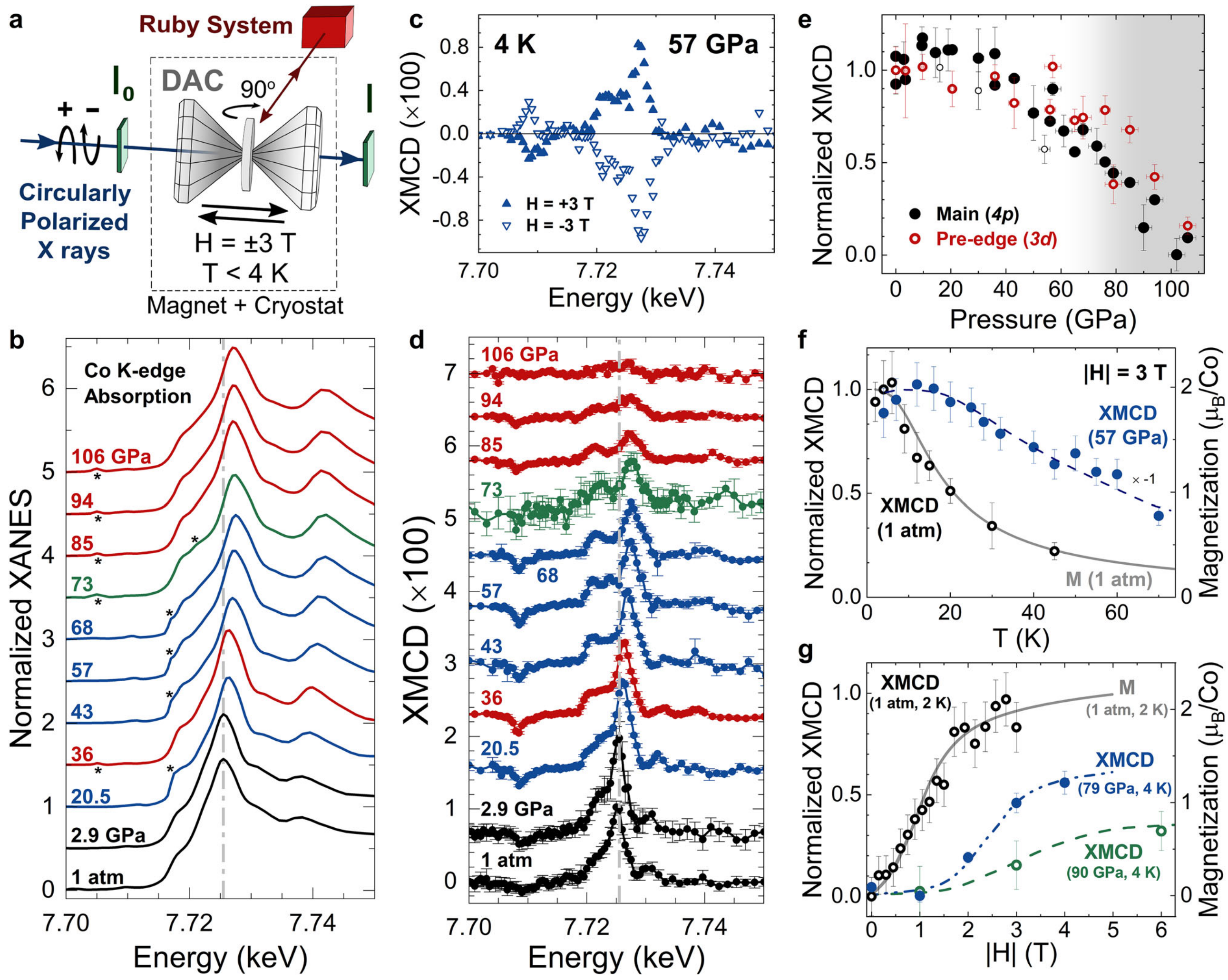

Fig. 2 | Evolution of electronic structure and spin correlations probed with x-ray absorption and magnetic circular dichroism. **a** Experimental setup for x-ray absorption near edge structure (XANES) and x-ray magnetic circular dichroism (XMCD) experiments; see methods for details. **b** Selected Co K-edge normalized XANES and **c**, **d** corresponding XMCD as a function of pressure for a powder sample at $|H| = 3$ T. Data in (**d**) were obtained by subtracting and halving XMCD data for opposite field directions. Ambient pressure data were collected at 2 K; data at other pressures at 4 K. Different colors denote different experimental runs; pressure values given in GPa units. Vertical dashed and dotted lines at 7.726 keV in (**b**, **d**) are guides to the eye. Star (*) symbols on XANES spectra indicate contamination signal from Bragg peaks in diamond anvils. **e** Integrated XMCD signals, normalized to 1 atm values, for the pre-edge (red open circles) and "white line" (closed black circles). The spin transition region, between about 60 and 90 GPa, is shown in gradient color bridging the white (HS) and gray (LS) regions. **f** Temperature dependence of integrated XMCD signal at 1 atm and 57 GPa. **g** Field dependence of integrated XMCD signal at 1 atm, 79 GPa, and 90 GPa. In (**f**, **g**), ambient pressure magnetometry data (SQUID, solid lines) are displayed on the right axis. Normalized XMCD at 1 atm was scaled to match the magnetization data. Dashed lines are guides to the eye. Vertical error bars in panel (**d**) are standard deviations from the average of independent scans, then propagated in data integrals shown in panels (**e**–**g**). Horizontal error bars in (**e**) are pressure gradients over the illuminated sample volume.

lower temperatures, are shown with black lines in Fig. 3b. The presence of an intense Kβ' satellite at ambient pressure is as expected for the HS $S = \frac{3}{2}$ configuration of Co^{2+} ions. XES difference spectra relative to 5 GPa (Fig. 3d) highlight the changes in both primary line emission energy and intensity, as well as satellite intensity. The integrated relative difference (IRD), shown in Fig. 3e, is the integral of the difference spectra over the energy range encompassing the satellite peak[45–47]. The intensity of the Kβ' satellite decreases slowly up to about 60 GPa, likely a result of reduced intra-atomic $3p$ –$3d$ overlap from increased delocalization of $3d$ valence electrons under compression. At pressures above 60 GPa a sudden acceleration in the loss of satellite intensity is observed, which we interpret to signal a spin transition from HS ($S = \frac{3}{2}$) to LS ($S = \frac{1}{2}$) state (see also Supplementary Note 3 and Fig. S9). Theoretical simulations of XES spectra, difference spectra, and IRD intensities using cluster calculations are shown with red lines and open circles alongside their experimental counterparts in b, d, e panels of Fig. 3. A spin transition will take place when the HS state, which maximizes the total spin of t_{2g} and e_g orbitals (Hund's first rule) is no longer energetically favorable in the presence of an increasing octahedral crystal field that raises the energy of doubly populated e_g states under compression, leading to a more favorable $t_{2g}^6 e_g^1$ LS configuration. Figure 3f shows numerical calculations of hole occupancies, while Fig. 3g shows the related evolution of expectation values $\langle S_z \rangle$, $\langle L_z \rangle$, and $\langle \mathbf{L} \cdot \mathbf{S} \rangle$ for Co $3d$ electrons. As expected, the orbital angular momentum nearly vanishes in the low-spin state due to full occupation of $l_{\mathrm{eff}} = 1$, t_{2g} states. DFT+U calculations find a HS-LS transition at about 70 GPa (see Supplementary Note 4 and Fig. S11). Inclusion of spin-orbit coupling (SOC) in DFT + U + SOC calculations yields a similar pressure for the spin transition, as well as spin and orbital moment values which are in reasonable agreement with those from cluster calculations (see Supplementary Fig. S12).

The decrease of magnetic susceptibility above 60 GPa is driven by the spin transition, as seen in the correlated suppression of XMCD and XES signals (see Supplementary Fig. S10a). The experimental transition width

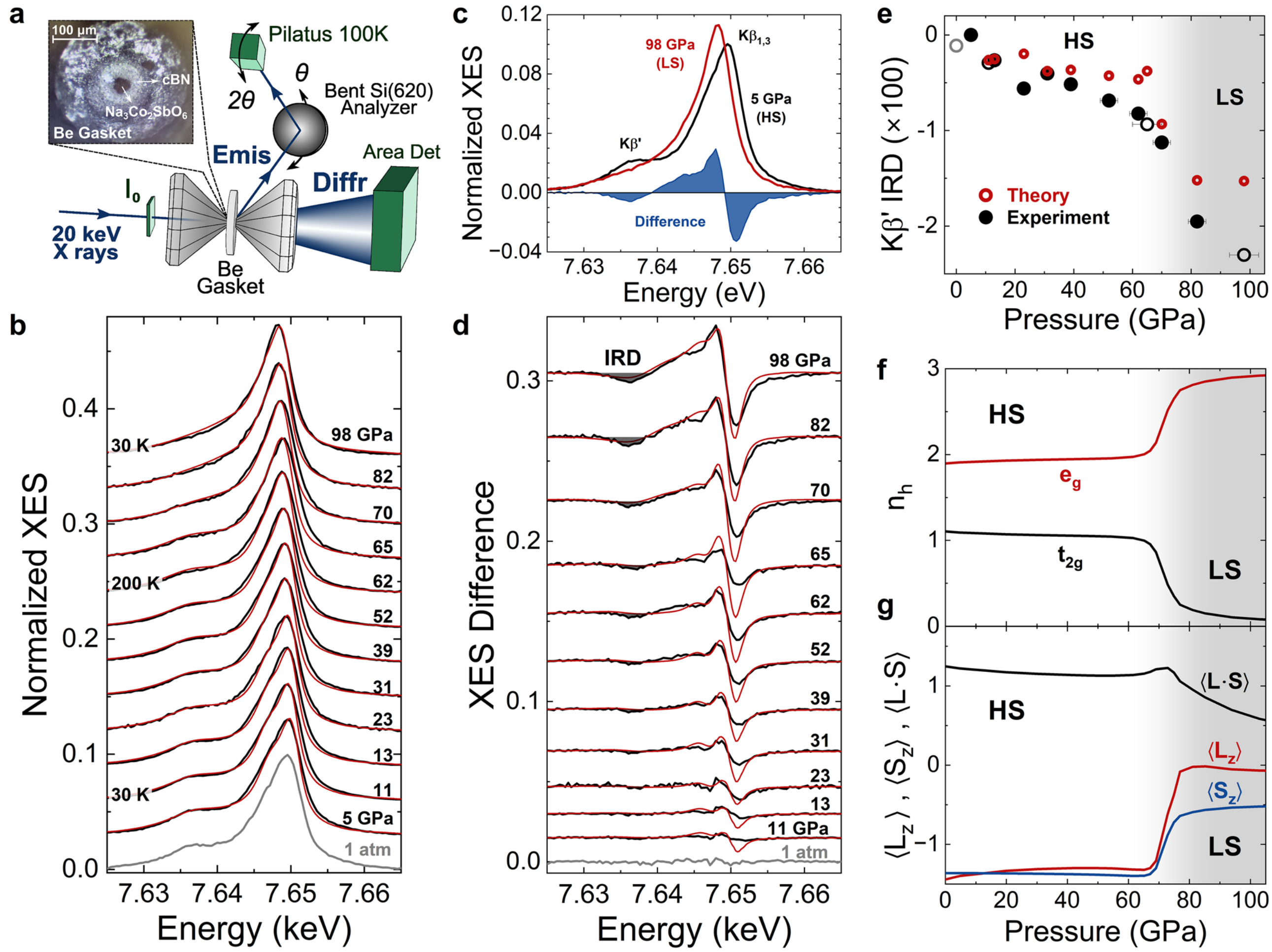

Fig. 3 | Evolution of spin moment probed with x-ray emission spectroscopy. **a** Experimental setup for high-pressure x-ray emission spectroscopy (XES); see methods for details. **b** Area-normalized experimental (black) and theoretical (red lines) Co Kβ emission spectra. Data were collected mostly at room temperature, with some spectra collected at lower temperatures as labeled. The 65 GPa data were collected during decompression. **c** Comparison between HS and LS spectra. **d** Difference in XES spectra relative to the 5 GPa spectra (lowest pressure in the DAC). Black lines are experiment; red lines theory. **e** XES integrated relative differences (IRD) as a function of pressure. Experimental (black circles) and theoretical (open red circles) data show a drop around 60–70 GPa signaling the beginning of a spin transition from HS (white region) to LS (gray region). Open black circles indicate experimental data collected at temperatures different from ambient, and the open gray circle represents 1 atm data collected outside of the DAC. **f** Calculated number of holes in Co e_g and t_{2g} states and **g** expectation values $\langle S_z \rangle$, $\langle L_z \rangle$ and $\langle \mathbf{L} \cdot \mathbf{S} \rangle$ for Co 3*d* electrons. Vertical error bars in panel (**b**–**e**), smaller than line thickness at the Kβ' energy, and smaller than symbols, are standard deviations from the average of independent scans, then propagated in data differences and integrals. Horizontal error bars in (**e**) are pressure gradients over the illuminated sample volume.

spans a change in reduced volume of about 5% (see Supplementary Fig. S10b), which is similar to the 7-8% span seen in $PbCoO_3$[38]. The spin transition width has both extrinsic and intrinsic contributions. Pressure gradients, reported in the "Methods" section, contribute to the finite width due to the coexistence of HS and LS states in different parts of the illuminated sample. Intrinsic contributions involve coupling between HS and LS states on the same Co site when their energies become proximate under pressure. The intrinsic width is determined by the energy scale of the mixing interaction(s). In the cluster calculations, a one-particle spin-orbit interaction of 66 meV leads to the finite width shown in Fig. 3f. The similar transition widths seen in XMCD ($T = 4$ K) and XES ($T = 300$ K) data, as well as no significant difference in XES spectra for selected pressures at 30 K and 300 K (Fig. 3e), indicate that 300 K is not sufficiently high to contribute significant broadening to the transition. While DFT calculations are bound to yield rather sharp spin transitions when the LS state becomes energetically favorable (see Supplementary Figs. S11b and S12), extensions to dynamical mean field theory (DMFT) account for local dynamic electronic effects and lead to transition widths similar to experiment[48].

The LS $t_{2g}^6 e_g^1$ state is expected to be Jahn-Teller active. DFT+U calculations show enhanced splitting of Co-O distances across the spin transition, consistent with Jahn-Teller distortion (see Supplementary Fig. S11). A cooperative Jahn-Teller distortion may lead to a lowering of lattice symmetry in the LS state that could go undetected in our XRD data due to peak broadening at the highest pressures. We speculate that such cooperative Jahn-Teller distortion, which may entail ordering of $d_{x^2-y^2}$ and d_{z^2} orbitals, could contribute to the apparent slow-down of energy shifts in XANES spectra at the spin transition (see Supplementary Fig. S5) as well as counteract the effect of a local volume contraction that is expected from the reduced atomic volume of LS divalent Co ions[37]. Single crystal XRD[49], neutron diffraction[50], and optical Raman scattering[51] could provide additional insight into a possible lowering of crystal symmetry in the LS state.

Charge-transfer gap

$Na_3Co_2SbO_6$ is a charge-transfer insulator in which the lowest charge excitation is dictated by the energy separation, Δ_{pd}, between occupied O 2*p* and unoccupied Co 3*d* states. This charge-transfer gap, of order 2–3 eV, as well as the larger 3*d*–3*d* ($U_{dd} \sim 5$–8 eV) excitation gap, are expected to stabilize the insulating state to pressures above the Mbar regime. An insulating state is required to stabilize the KQSL state, where charge degrees of freedom are frozen out and the lowest energy physics is dictated by fractionalized spin excitations. Since suppression of spin correlations at the highest pressure can also be a result of metallization, we carried out synchrotron infrared (IR) spectroscopy in both the far (FIR) and mid (MIR) ranges. IR absorbance data are shown in Fig. 4. A metallic sample has perfect reflectivity for energies below the plasmon energy, $\hbar\omega_p$ (typically 5–10 eV). Absorbance data, computed as $\log(I_0/I)$ where I_0 is background intensity without sample and I is transmitted intensity, is expected to diverge for $\omega \ll \omega_p$ as transmittance drops to zero (see Supplementary Note 5). The FIR data shows phonon excitations that stiffen under pressure at a rate of ~3.6(1) $\mathrm{cm^{-1}\,GPa^{-1}}$ (see Supplementary Fig. S13). Otherwise, the spectra reveal a high transmittance down to 20 meV with no signature of a Drude response from metallization. The MIR data reinforces this conclusion, not only by the lack of a Drude response to 111 GPa, but also from the absence of a closing charge-transfer gap excitation moving from the optical into the IR regime (multiple runs and full MIR data sets are shown in Supplementary Fig. S13). The MIR data set a lower limit of ~1 eV for the charge-transfer gap at the highest pressure of 111 GPa.

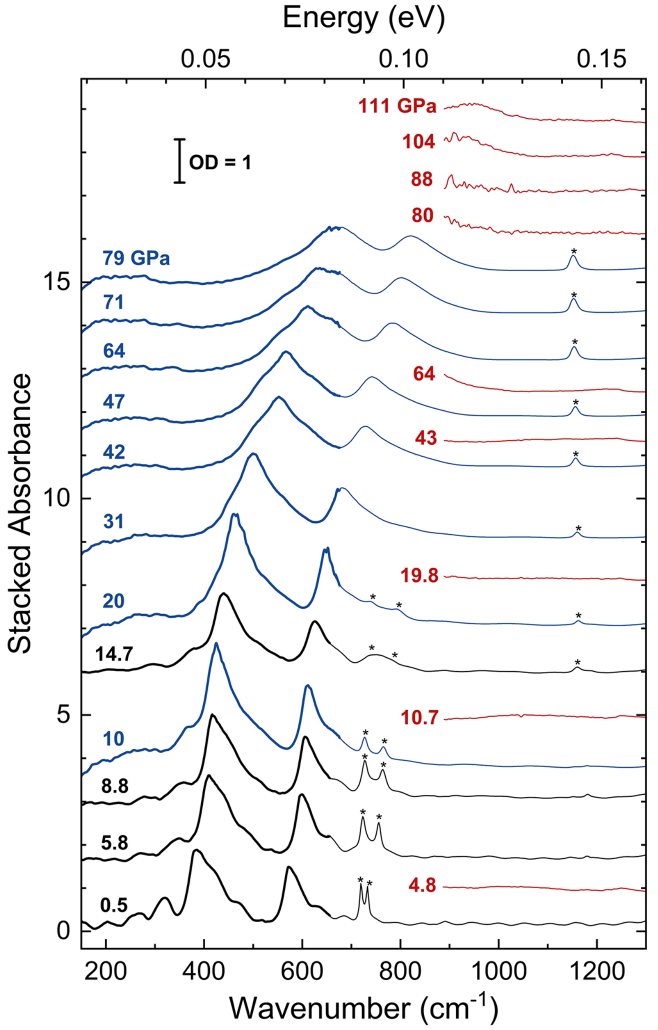

Fig. 4 | Absence of pressure-induced metallization probed with infrared spectroscopy. Selected synchrotron far infrared (FIR) and mid infrared (MIR) absorbance spectra as a function of pressure, shown with dark and faint lines, respectively. The scale bar on top denotes the absorbance value of unity. Spectra are offset in the vertical direction for clarity. Different colors represent different experimental runs. * symbols denote excitations in the pressure transmitting medium (petrol jelly) in two of the runs. These peaks are absent on the third run, where KBr medium was used instead.

Discussion

The $J_{\mathrm{eff}} = \frac{1}{2}$ pseudospin wavefunction, and related superexchange interactions between pseudospins mediated by oxygen ions, depend on the size of the trigonal distortion of $\mathrm{CoO_6}$ octahedra[8], which XRD shows is significantly reduced with pressure. Superexchange interactions are also influenced by the degree of covalency/mixing between Co 3d and O 2p orbitals, which is also modified upon lattice compression. Based on the predictions of Liu et al.[8], a reduction in the trigonal crystal field should move $\mathrm{Na_3Co_2SbO_6}$ towards the KQSL state. Since Kitaev exchange interactions in this cobaltate are expected to be ferromagnetic[8,10,11], one may be tempted to assign the enhanced ferromagnetic correlations observed below 60 GPa, where the $J_{\mathrm{eff}} = \frac{1}{2}$ character of the pseudospin is preserved, to dominant Kitaev interactions. However, field-induced low-temperature magnetization near full moment values, which persists to rather high temperatures, is inconsistent with enhanced frustration. A likely explanation for the increased ferromagnetic correlations is pressure-induced enhancement of ferromagnetic $e_g - e_g$ isotropic superexchange interactions relative to the antiferromagnetic t_{2g}–e_g superexchange, driven by increased covalency. Evidence for increased covalency is seen in the XES-IRD data which display a gradual reduction in intensity within the HS state below 60 GPa (Fig. 3e). A near cancellation of isotropic ferro- and antiferromagnetic exchange interactions at ambient pressure is predicted to make this cobaltate proximate to a KQSL[8], the sizable trigonal distortion preventing its full realization. Although the trigonal distortion is strongly reduced, a disruption in the balance of isotropic exchange interactions as a result of covalency will drive this cobaltate away from the KQSL limit at intermediate pressures.

We have assumed that the trigonal crystal field is dominated by the distortion of $\mathrm{CoO_6}$ octahedra, i.e., by the oxygen ligands. Instead, if the trigonal field from Sb ions in Co-Sb planes dominates and contributes with an opposite sign, as has been previously proposed[8] but recently challenged[13,52], removing the trigonal distortion of $\mathrm{CoO_6}$ octahedra will increase the non-cubic crystal field and tend to stabilize magnetically ordered phases[8]. An increase in the ratio of Mott-Hubbard U to charge-transfer gap, Δ_{pd}, under pressure can also contribute to an enhancement of non-Kitaev ferromagnetic correlations[8].

The spin transition above 70 GPa manifests a strong suppression of $T = 4$ K magnetic susceptibility, which vanishes at 100 GPa in a 3 T applied field. The localized 3d orbitals protect this honeycomb lattice from a dimerization transition, and therefore the mute susceptibility is not a result of the formation of molecular orbitals with spin-singlet states, typical of dimerized 4d/5d honeycombs[25,31,53,54]. Conventional antiferromagnetic ordering with gapped magnetic excitations can also lead to mute susceptibility and a similar field dependence to that measured at 90 GPa. However, first-neighbor exchange interactions between e_g spins in LS $\mathrm{Co^{2+}}$ ions are expected to be ferromagnetic[55,56], making this scenario less likely. The spin transition quenches the orbital angular momentum (filled t_{2g} states), destroying the spin-orbital $J_{\mathrm{eff}} = \frac{1}{2}$ pseudospin wavefunction required to map bond-directional exchange interactions into Kitaev's model. The emergence of strongly reduced, $S = 1/2$ moments in a 2D honeycomb lattice of LS $\mathrm{Co^{2+}}$ ions can lead to non-classical magnetic ground states as a result of strong quantum fluctuations. A $J_1 - J_3$ ferro-antiferromagnetic XXZ quantum $S = \frac{1}{2}$ model on the honeycomb lattice[32], where $J_1 < 0$ is ferromagnetic as expected for nearest-neighbor interactions between e_g spins, reveals a non-classical Ising-z phase near the XY limit and $J_3/J_1 \sim -0.35$. It features compensated spins perpendicular to the honeycomb plane despite dominant in-plane exchange interactions, an example of quantum order by disorder. A study of the isotropic $J_1 - J_2$ quantum $S = \frac{1}{2}$ model on the honeycomb lattice with ferromagnetic $J_1 < 0$ yields a gapped quantum spin liquid phase with short-ranged dimer-dimer correlations at $J_2/J_1 \sim -0.25$[33]. In the absence of metallization, as clearly established by IR spectroscopy, exchange correlations between $S = \frac{1}{2}$ moments are expected to stabilize magnetic order at low temperature unless quantum fluctuations are at play. The muted susceptibility alongside its field-dependence measured in the LS state (Fig. 2e, g) is consistent with emergent quantum paramagnetism as a result of frustrated exchange interactions between localized $S = \frac{1}{2}$ spins as found in $J_1 - J_2 - J_3$ quantum models in honeycomb lattices[32,33]. The measurement uncertainties at low applied fields prevent asserting whether such a paramagnetic state is gapped or gapless. Further technical developments are needed to probe spin correlations and excitations into the Mbar range, e.g., with inelastic neutron scattering[57,58], optical Raman scattering[59], or NMR techniques[60] in order to provide additional insight into the complex quantum magnetism of highly compressed $Na_3Co_2SbO_6$.

Methods

Sample synthesis

Polycrystalline samples were synthesized in the Materials Science Division at Argonne National Laboratory following the procedures described in ref. 14. Laboratory powder XRD confirmed the single-phase nature of the samples. Magnetic susceptibility measurements at ambient pressure confirmed antiferromagnetic ordering below $T_N = 8$ K (see Supplementary Fig. S4). Single-crystalline samples were prepared at Oak Ridge National Laboratory as described in ref. 20, and displayed a Néel temperature $T_N \sim 5$ K. The reduced ordering temperature relative to powder samples was attributed to the significant presence of stacking faults, promoted by the vapor transport growth method[20]. Improvements in single crystal growth using the flux method are now yielding T_N values within ~1 K of those in powder samples[15].

X-ray diffraction

Diffraction measurements were performed at the Advanced Photon Source (APS), Argonne National Laboratory, using the High-Pressure Collaborative Access Team (HPCAT) beamlines 16-BM-D and 16-ID-D[61]. X-ray energies were 30 and 29.2 keV, respectively. Measurements were performed at 300, 240, 15, and 8 K under variable pressures up to 108 GPa. Complete data sets are shown in Supplemental Fig. S1. Symmetric diamond anvil cells (DACs) were mounted with either 100, 180, or 300 μm-culet diamond anvils depending on the pressure range aimed for the run. Re gaskets were indented to a thickness of about 1/5 of the culet diameter, and a hole was laser drilled in the center of the indentation with a diameter between 1/3 and 1/2 of the culet size[62]. DACs with 100 μm-culet anvils were gas loaded[63] with He and used ruby luminescence[64,65] together with Raman spectroscopy of diamond[66,67] for pressure calibration. DACs with 180 μm and 300 μm anvils had either helium or neon as pressure medium, with both ruby and gold as pressure markers. Loose powder with a grain size of about 1 μm was loaded without filling the entire sample chamber to achieve a reasonable sample-medium ratio for better hydrostaticity. Beam dimensions in all runs were around $5 \times 5\ \mu m^2$ (FWHM), but the full width at 1% of maximum intensity was around $25 \times 25\ \mu m^2$. Diffraction patterns were integrated using Dioptas[68] and Le Bail fitted using Jana2020[69] in order to get lattice parameters as a function of pressure. Volume at 1 atm, bulk modulus and its pressure derivative were obtained using the EosFit7 software[70].

X-ray magnetic circular dichroism

Co K-edge XMCD measurements were performed at APS beamline 4-ID-D[71], using loose powder loaded in CuBe DACs with ruby pressure marker[64,65] in neon medium[63]. Fully perforated, partially perforated and full anvils were used for experiments up to 106 GPa. 100, 180 and 300 μm-culet diamonds were employed in 4 different experimental runs, in which Re gaskets were indented to a thickness of about 1/5 of the culet diameter, and a hole was laser drilled in the center of the indentation with a diameter between 1/3 and 1/2 of the culet size[62]. Compression and decompression gas membranes were attached to the DAC body to allow for pressure stability during cool downs and for reversibility studies. Pressure was calibrated before and after measurements at each pressure point, via a ruby system composed of a 473 nm laser, spectrometer and focusing optics. This system inserts into the reentrant room temperature bore between the split, longitudinal field magnet coils of a 6.5 Tesla cryomagnet, giving optical access to ruby fluorescence after rotating the DAC by ~90° inside the magnet. Sample is cooled in ^{4}He vapor. K-B mirrors were employed in the 3 last runs, which significantly improved signal-to-noise ratio in comparison with the first run (300 μm culets). The small sample volume used with 100 μm anvils (initial gasket indentation of about 20 μm) was the main source of noise for the highest pressures (reduced absorption edge jump). A combination of helicity switching of circularly polarized x-rays and magnetic field switching was used to obtain clean XMCD spectra and mitigate the contribution of artifacts. On average, each pressure point took from 8 to 10 hours to complete. Experiments were run at $|H| = 3$ T and 2 K for pressures below 9.6 GPa. For all other pressure points, experiments were run at 4 K to avoid freezing of Helium in the compression and decompression membranes. Pressure gradients were about ±3 GPa at the highest pressure.

X-ray emission spectroscopy

High-pressure Co Kβ XES experiments were performed at HPCAT's beamline 16-ID-D, using 20 keV x-rays and a symmetric DAC in a diamond-in, gasket-out geometry. The DAC was placed inside a cryostat, pressure was applied using a gas membrane and XES data were collected through a side window after diffraction from a bent Si(620) analyzer. Single-beveled 100 μm-culet diamonds were used to indent a Be gasket to a thickness of about 20 μm. A hole of 98 μm was laser drilled on the indentation, and the region was filled with a properly cured 10:1 cBN:epoxy (EPO-TEK 353ND) mixture[72,73]. After packing, the cBN mixture formed a robust insert that was laser drilled to create the sample space, a 30 μm-diameter hole. Fine (<1 μm grain size) loose powder was loaded, and silicone oil was used as a pressure medium. X-ray diffraction was collected through the downstream cryostat window in forward scattering geometry using a Pilatus 100K detector. Pressure was calibrated using the (001) peak and the equation of state shown in Fig. 1b. All XES data were analyzed using the integrated relative difference (IRD) method[45,47] with focus on the pressure-dependent behavior of the satellite peak at ~7.636 keV (see Supplementary Note 3). Pressure gradients were about ± 5 GPa at the highest pressure.

Infrared absorption spectroscopy

Infrared absorption spectra were collected at the Frontier Synchrotron Infrared Spectroscopy (FIS) beamline, 22-IR-1, Brookhaven National Laboratory (BNL). Absorbance, defined as $A = \log(I_0/I)$, where I_0 is the reference spectrum or background intensity and I is the intensity of infrared light transmitted through the sample, was measured using single-crystal samples[20]. High-pressure absorbance was measured in multiple runs using different DAC loadings covering the far infrared (FIR, < 650 cm^{-1}) and mid infrared (MIR, 650–8000 cm^{-1}) regions. Petrol jelly was used as a pressure-transmitting medium for the FIR region, and KBr for the MIR measurements. Due to different experimental setups, I_0 in the FIR region is measured by transmitting through the diamond anvils only (taken once at 1 atm before the sample is loaded), while in the MIR region, it is measured through both diamonds and KBr at each pressure point.

Density functional theory

We adopted Density Functional Theory plus Hubbard U (DFT + U)[74] based on the projected-augmented wave (PAW) method[75] as implemented in the Vienna ab initio simulation package (VASP)[76,77]. The exchange-correlation energy functional was treated using generalized gradient approximation (GGA) by adopting the Perdew-Burke-Ernzerhof (PBE) functional[78]. We used the cutoff energy for the plane-wave basis as 600 eV, and the Gamma-centered $8 \times 4 \times 8$ k-point. To treat the correlation effect of Co 3d orbitals, we impose the Hubbard U and the Hund's coupling J within DFT + U with $U = 5$ eV and $J = 0.8$ eV. Calculations were done both by relaxing atomic positions at different pressures while keeping lattice parameters fixed to their experimental values, as well as relaxing lattice parameters and atomic positions while keeping the unit cell volumes fixed to their experimental values. The Hellmann-Feynman force on each atom was set to be smaller than 0.01 eV Å^{-1} for convergence. Spin-orbit coupling (SOC) was included in DFT + U + SOC calculations to investigate the pressure evolution of spin and orbital moments. These calculations used the same relaxed structures and parameters (U, J, k-point grid, energy cutoff, and exchange-correlation functional) of DFT + U calculations, albeit with convergence criteria of 10^{-7} instead of 10^{-4}. A collinear Néel AFM structure was used as a starting point for all DFT calculations, with Co moments lying on the *ab*-plane.

Cluster calculations

In order to describe the Kβ spectral lineshapes and the ground-state expectation values, calculations were performed on a divalent cobalt ion. To describe the local electronic structure on cobalt, the same approach is followed as in refs. [14,79] but a CoO_6 is used in this case instead of a cobalt ion. The Hamiltonian includes the Coulomb and spin-orbit interactions. The effect of the ligands is included by an effective crystal field, $10Dq$. The trigonal crystal field interaction was not included as it is much weaker than $10Dq$ and Coulomb interactions driving the spin transition. The Kβ spectra are obtained by calculating the $3p \rightarrow 1s$ radiative decay[80]. The crystal field values were converted to pressure using the following conditions. The $10Dq$ value at ambient pressure is 1.1 eV, which is obtained from a detailed fit of the L-edge x-ray absorption spectra[14]. The spin crossover occurs at $10Dq \cong 2.27$ eV. The change in Co-O distances d should follow the behavior of the lattice parameters. The crystal field depends on the lattice parameters as $(d_0/d)^a$ where d_0 is the distance at ambient pressure[81]. In order to satisfy these conditions, a value of $a \cong 5$ is needed. This is close to the expected power for a change in the crystal field due to a change in metal-ligand distance.

Data availability

Numerical data used to generate all figures, as well as refined structures (.cif files), can be obtained from the Zenodo data repository (https://doi.org/10.5281/zenodo.14052640). Raw data can be obtained by contacting Daniel Haskel at haskel@anl.gov.

Received: 5 March 2025; Accepted: 3 June 2025;

References

1. Kitaev, A. Anyons in an exactly solved model and beyond. *Ann. Phys.* **321**, 2–111 (2006).
2. Kitaev, A. Y. Fault-tolerant quantum computation by anyons. *Ann. Phys.* **303**, 2–30 (2003).
3. Freedman, M. H., Larsen, M. & Wang, Z. A modular functor which is universal for quantum computation. *Commun. Math. Phys.* **227**, 605–622 (2002).
4. Nayak, C., Simon, S. H., Stern, A., Freedman, M. & Sarma, S. D. Non-abelian anyons and topological quantum computation. *Rev. Mod. Phys.* **80**, 1083 (2008).
5. Kim, B. J. et al. Novel J_{eff}=1/2 Mott state induced by relativistic spin-orbit coupling in Sr_2IrO_4. *Phys. Rev. Lett.* **101**, 076402 (2008).
6. Jackeli, G. & Khaliullin, G. Mott insulators in the strong spin-orbit coupling limit: From Heisenberg to a quantum compass and Kitaev models. *Phys. Rev. Lett.* **102**, 017205 (2009).
7. Takagi, H., Takayama, T., Jackeli, G., Khaliullin, G. & Nagler, S. E. Concept and realization of kitaev quantum spin liquids. *Nat. Rev. Phys.* **1**, 264 (2019).
8. Liu, H., Chaloupka, J. & Khaliullin, G. Kitaev spin liquid in 3*d* transition metal compounds. *Phys. Rev. Lett.* **125**, 047201 (2020).
9. Liu, H. & Khaliullin, G. Pseudospin exchange interactions in d^7 cobalt compounds: possible realization of the Kitaev model. *Phys. Rev. B* **97**, 014407 (2018).
10. Sano, R., Kato, Y. & Motome, Y. Kitaev-Heisenberg Hamiltonian for high-spin d^7 Mott insulators. *Phys. Rev. B* **97**, 014408 (2018).
11. Songvilay, M. et al. Kitaev interactions in the Co honeycomb antiferromagnets $Na_3Co_2SbO_6$ and $Na_2Co_2TeO_6$. *Phys. Rev. B* **102**, 224429 (2020).
12. Yao, W., Iida, K., Kamazawa, K. & Li, Y. Excitations in the ordered and paramagnetic states of honeycomb magnet $Na_2Co_2TeO_6$. *Phys. Rev. Lett.* **129**, 147202 (2022).
13. Kim, C. et al. Antiferromagnetic Kitaev interaction in J_{eff} = 1/2 cobalt honeycomb materials $Na_3Co_2SbO_6$ and $Na_2Co_2TeO_6$. *J. Phys.: Condens. Matter* **34**, 045802 (2022).
14. van Veenendaal, M. et al. Electronic structure of Co 3*d* states in the Kitaev material candidate honeycomb cobaltate $Na_3Co_2SbO_6$ probed with x-ray dichroism. *Phys. Rev. B* **107**, 214443 (2023).
15. Gu, Y. et al. In-plane multi-q magnetic ground state of $Na_3Co_2SbO_6$. *Phys. Rev. B* **109**, L060410 (2024).
16. Halloran, T. et al. Geometrical frustration versus Kitaev interactions in $BaCo_2(AsO_4)_2$. *Proc. Natl Acad. Sci. USA* **120**, e2215509119 (2023).
17. Banerjee, A. et al. Proximate Kitaev quantum spin liquid behaviour in a honeycomb magnet. *Nat. Mater.* **15**, 733 (2016).
18. Wolter, A. U. B. et al. Field-induced quantum criticality in the Kitaev system α-$RuCl_3$. *Phys. Rev. B* **96**, 041405 (2017).
19. Viciu, L. et al. Structure and basic magnetic properties of the honeycomb lattice compounds $Na_2Co_2TeO_6$ and $Na_3Co_2SbO_6$. *J. Solid State Chem.* **180**, 1060–1067 (2007).
20. Yan, J.-Q. et al. Magnetic order in single crystals of $Na_3Co_2SbO_6$ with a honeycomb arrangement of $3d^7$ Co^{2+} ions. *Phys. Rev. Mat.* **3**, 074405 (2019).
21. Vavilova, E. et al. Magnetic phase diagram and possible Kitaev-like behavior of the honeycomb-lattice antimonate $Na_3Co_2SbO_6$. *Phys. Rev. B* **107**, 054411 (2023).
22. Hu, Z. et al. Field-induced phase transitions and quantum criticality in the honeycomb antiferromagnet $Na_3Co_2SbO_6$. *Phys. Rev. B* **109**, 054411 (2024).
23. Li, X. et al. Giant magnetic in-plane anisotropy and competing instabilities in $Na_3Co_2SbO_6$. *Phys. Rev. X* **12**, 041024 (2022).
24. Zhang, X. et al. A magnetic continuum in the cobalt-based honeycomb magnet $BaCo_2(AsO_4)_2$. *Nat. Mater.* **22**, 58–63 (2023).
25. Takayama, T. et al. Competing spin-orbital singlet states in the $4d^4$ honeycomb ruthenate $Ag_3LiRu_2O_6$. *Phys. Rev. Res.* **4**, 043079 (2022).
26. Hermann, V. et al. Pressure-induced formation of rhodium zigzag chains in the honeycomb rhodate Li_2RhO_3. *Phys. Rev. B* **100**, 064105 (2019).
27. Xu, Y. et al. Pressure-induced structural evolution with a turnover point in the honeycomb iridate Na_2IrO_3. *J. Phys. Chem. C* **127**, 20177–20182 (2023).
28. Shen, B. et al. Interplay of magnetism and dimerization in the pressurized Kitaev material β-Li_2IrO_3. *Phys. Rev. B* **104**, 134426 (2021).
29. Veiga, L. S. I. et al. Pressure-induced structural dimerization in the hyperhoneycomb iridate β-Li_2IrO_3 at low temperatures. *Phys. Rev. B* **100**, 064104 (2019).
30. Fabbris, G. et al. Complex pressure-temperature structural phase diagram of the honeycomb iridate Cu_2IrO_3. *Phys. Rev. B* **104**, 014102 (2021).
31. van Veenendaal, M. & Haskel, D. Interpretation of Ir L-edge isotropic x-ray absorption spectra across the pressure-induced dimerization transition in hyperhoneycomb β-Li_2IrO_3. *Phys. Rev. B* **105**, 214420 (2022).
32. Jiang, S., White, S. R. & Chernyshev, A. L. Quantum phases in the honeycomb-lattice J1-J3 ferro-antiferromagnetic model. *Phys. Rev. B* **108**, L180406 (2023).
33. Fouet, J. B., Sindzingre, P. & Lhuillier, C. An investigation of the quantum J1-J2-J3 model on the honeycomb lattice. *Eur. Phys. J. B* **20**, 241–254 (2001).
34. Birch, F. Elasticity and constitution of the earth's interior. *J. Geophys. Res.* **57**, 227 (1952).
35. Vinet, P., Ferrante, J., Smith, J. R. & Rose, J. H. A universal equation of state for solids. *J. Phys. C Solid State Phys.* **19**, L467 (1986).
36. Vinet, P., Smith, J. R., Ferrante, J. & Rose, J. H. Temperature effects on the universal equation of state of solids. *Phys. Rev. B* **35**, 1945–1953 (1987).

37. Shannon, R. D. Revised effective ionic radii and systematic studies of interatomic distances in halides and chaleogenides. *Acta Cryst.* **A32**, 751–767 (1976).
38. Liu, Z. et al. Sequential spin state transition and intermetallic charge transfer in $PbCoO_3$. *J. Am. Chem. Soc.* **142**, 5731–5741 (2020).
39. Guo, Q., Mao, H.-K., Hu, J., Shu, J. & Hemley, R. J. The phase transitions of CoO under static pressure to 104 GPa. *J. Phys. Condens. Matter* **14**, 11369–11374 (2002).
40. Rueff, J.-P., Mattila, A., Badro, J., Vankó, G. & Shukla, A. Electronic properties of transition-metal oxides under high pressure revealed by x-ray emission spectroscopy. *J. Phys. Condens. Matter* **17**, S717–S726 (2005).
41. Robinson, K., Gibbs, G. V. & Ribbe, P. H. Quadratic elongation: a quantitative measure of distortion in coordination polyhedra. *Science* **172**, 567–570 (1971).
42. Tsutsumi, K. The x-ray non-diagram lines Kβ' of some compounds of the iron group. *J. Phys. Soc. Japan* **14**, 12 (1959).
43. Tsutsumi, K. & Nakamori, H. X-ray K emission spectra of chromium in various chromium compounds. *J. Phys. Soc. Japan* **25**, 5 (1968).
44. Sikora, M. et al. Strong K-edge magnetic circular dichroism observed in photon-in-photon-out spectroscopy. *Phys. Rev. Lett.* **105**, 037202 (2010).
45. Li, N. et al. Structural and electronic phase transitions of $Co_2Te_3O_8$ spiroffite under high pressure. *Phys. Rev. B* **99**, 245125 (2019).
46. Yoo, C. S. et al. First-order isostructural mott transition in highly compressed MnO. *Phys. Rev. Lett.* **94**, 115502 (2005).
47. Mao, Z. et al. Spin and valence states of iron in Al-bearing silicate glass at high pressures studied by synchrotron mössbauer and x-ray emission spectroscopy. *Am. Min.* **99**, 415–423 (2014).
48. Kunes, J., Lukoyanov, A. V., Anisimov, V. I., Scalettar, R. T. & Pickett, W. E. Collapse of magnetic moment drives the mott transition in MnO. *Nat. Mater.* **7**, 198–202 (2008).
49. Ji, C. et al. Ultrahigh-pressure isostructural electronic transitions in hydrogen. *Nature* **573**, 558 (2019).
50. Haberl, B., Guthrie, M. & Boehler, R. Advancing neutron diffraction for accurate structural measurement of light elements at megabar pressures. *Sci. Rep.* **13**, 4741 (2023).
51. Baldini, M., Struzhkin, V. V., Goncharov, A. F., Postorino, P. & Mao, W. L. Persistence of Jahn-Teller distortion up to the insulator to metal transition in $LaMnO_3$. *Phys. Rev. Lett.* **106**, 066402 (2011).
52. Kim, G.-H. et al. Suppression of antiferromagnetic order by strain-enhanced frustration in honeycomb cobaltate. *Sci. Adv.* **10**, eadn8694 (2024).
53. Takayama, T. et al. Pressure-induced collapse of the spin-orbital mott state in the hyperhoneycomb iridate β-Li_2IrO_3. *Phys. Rev. B* **99**, 125127 (2019).
54. Clancy, J. P. et al. Pressure-driven collapse of the relativistic electronic ground state in a honeycomb iridate. *npj Quant. Mater.* **3**, 35 (2018).
55. Kanamori, J. Superexchange interaction and symmetry properties of electron orbitals. *J. Phys. Chem. Solids* **10**, 87–98 (1959).
56. Goodenough, J. B. *Magnetism and the Chemical Bond*. (Interscience-Wiley, New York, 1963).
57. Zaliznyak, I. A., Dender, D. C., Broholm, C. & Reich, D. H. Tuning the spin hamiltonian of $Ni(C_2H_8N_2)_2NO_2ClO_4$ by external pressure: a neutron-scattering study. *Phys. Rev. B* **57**, 5200 (1998).
58. Pajerowski, D. M., Podlesnyak, A. P., Herbrych, J. & Manson, J. High-pressure inelastic neutron scattering study of the anisotropic $S=1$ spin chain $[Ni(HF_2)(3\text{-Clpyradine})_4]BF_4$. *Phys. Rev. B* **105**, 134420 (2022).
59. Li, X. et al. Magnetic order, disorder, and excitations under pressure in the Mott insulator Sr_2IrO_4. *Phys. Rev. B* **104**, L201111 (2021).
60. Haase, J., Goh, S. K., Meissner, T., Alireza, P. L. & Rybicki, D. High sensitivity nuclear magnetic resonance probe for anvil cell pressure experiments. *Rev. Sci. Instrum.* **80**, 073905 (2009).
61. Shen, G. et al. HPCAT: an integrated high-pressure synchrotron facility at the Advanced Photon Source. *High Press. Res.* **28**, 145–162 (2008).
62. Dunstan, D. J. Theory of the gasket in diamond anvil high pressure cells. *Rev. Sci. Instrum.* **60**, 3789–3795 (1989).
63. Rivers, M. et al. The COMPRES/GSECARS gas-loading system for diamond anvil cells at the Advanced Photon Source. *High Press. Res.* **28**, 273–292 (2008).
64. Barnett, J. D., Block, S. & Piermarini, G. J. An optical fluorescence system for quantitative pressure measurement in the diamond anvil cell. *Rev. Sci. Intrum.* **44**, 1–9 (1973).
65. Chijioke, A. D., Nellis, W. J., Soldatov, A. & Silvera, I. F. The ruby pressure standard to 150 Gpa. *J. Appl. Phys*. **98**, 114905 (2005).
66. Hanfland, M. & Syassen, K. A Raman study of diamond anvils under stress. *J. Appl. Phys.* **57**, 2752–2756 (1985).
67. Akahama, Y. & Kawamura, H. Pressure calibration of diamond anvil Raman gauge to 410 Gpa. *J. Phys. Conf. Ser.* **215**, 012195 (2010).
68. Prescher, C. & Prakapenka, V. B. DIOPTAS: a program for reduction of two-dimensional x-ray diffraction data and data exploration. *High Press. Res.* **35**, 223–230 (2015).
69. Petr^íček, V., Dušek, M. & Palatinus, L. Crystallographic computing system JANA2006: general features. *Z. Kristallogr*. **229**, 345–352 (2014).
70. Gonzalez-Platas, J., Alvaro, M., Nestolac, F. & Angel, R. EosFit7-GUI: a new graphical user interface for equation of state calculations, analyses and teaching. *J. Appl. Crystallogr.* **49**, 1377–1382 (2016).
71. Haskel, D., Tseng, Y. C., Lang, J. C. & Sinogeikin, S. Instrument for x-ray magnetic circular dichroism measurements at high pressures. *Rev. Sci. Instrum.* **78**, 083904 (2007).
72. Lin, J.-F., Shu, J., Mao, H.-K., Hemley, R. J. & Shen, G. Amorphous boron gasket in diamond anvil cell research. *Rev. Sci. Instrum.* **74**, 4732–4736 (2003).
73. Lin, J.-F. et al. Intermediate-spin ferrous iron in lowermost mantle post-perovskite and perovskite. *Nat. Geosci.* **1**, 688–691 (2008).
74. Liechtenstein, A. I., Anisimov, V. I. & Zaanen, J. Density-functional theory and strong interactions: Orbital ordering in Mott-Hubbard insulators. *Phys. Rev. B* **52**, R5467–R5470 (1995).
75. Blöchl, P. E. Projector augmented-wave method. *Phys. Rev. B* **50**, 17953–17979 (1994).
76. Kresse, G. & Furthmüller, J. Efficient iterative schemes for ab initio total-energy calculations using a plane-wave basis set. *Phys. Rev. B* **54**, 11169–11186 (1996).
77. Kresse, G. & Joubert, D. From ultrasoft pseudopotentials to the projector augmented-wave method. *Phys. Rev. B* **59**, 1758–1775 (1999).
78. Perdew, J. P., Burke, K. & Ernzerhof, M. Generalized gradient approximation made simple. *Phys. Rev. Lett.* **77**, 3865 (1996).
79. van Veenendaal, M. *The Theory of Inelastic Scattering and Absorption of X-rays*. (Cambridge University Press, Cambridge, 2015).
80. Wang, X., de Groot, F. M. F. & Cramer, S. P. Spin-polarized x-ray emission of 3*d* transition-metal ions: A comparison via Kα and Kβ detection. *Phys. Rev. B* **56**, 4553–4564 (1997).
81. Harrison, W. A. *Elementary Electronic Structure*. (World Scientific, Singapore, 1999).
82. Momma, K. & Izumi, F. VESTA 3 for three-dimensional visualization of crystal, volumetric and morphology data. *J. Appl. Cryst.* **44**, 1272–1276 (2011).

Acknowledgements

The authors thank Hide Takagi and Janice Musfeldt for helpful discussions. Work at the Advanced Photon Source (APS) and Materials Science Division of Argonne National Laboratory (ANL) was supported by the U.S. DOE Office of Science, Office of Basic Energy Sciences, under Contract No. DE-AC02-06CH11357. Work at UIC was supported by the U.S. National Science

Foundation (NSF, DMR-210488), the U.S. Department of Energy-National Nuclear Security Administration (DOE-NNSA) through the Chicago/DOE Alliance Center (DE-NA0004153), and the DOE Office of Science (DE-SC0020340). Portions of this work were performed at HPCAT (Sector 16) of APS at ANL. HPCAT operations are supported by DOE-NNSA's Office of Experimental Sciences. Helium and neon pressure media were loaded at GeoSoilEnviroCARS (The University of Chicago, Sector 13), APS, ANL. GeoSoilEnviroCARS is supported by NSF-Earth Sciences (EAR-1634415) and DOE-GeoSciences (DE-FG02-94ER14466). Crystal growth at ORNL was supported by the U.S. DOE, Office of Science, Basic Energy Sciences, Materials Sciences and Engineering Division. Neutron scattering research used resources at ORNL's High Flux Isotope Reactor, a DOE Office of Science User Facility, with beamtime allocated to the WAND^2 instrument. R.T. was supported by the São Paulo Research Foundation (FAPESP, 2019/10401-9 and 2022/03539-7). H.P. acknowledges the support by the Materials Sciences and Engineering Division, Basic Energy Sciences, Office of Science, US DOE. We acknowledge the computing resources provided on Bebop, a high-performance computing cluster operated by the Laboratory Computing Resource Center at ANL. This research used the 22-IR-1 beamline (FIS) of the National Synchrotron Light Source II, a U.S. Department of Energy (DOE) Office of Science User Facility operated for the DOE Office of Science by Brookhaven National Laboratory under Contract No. DE-SC0012704, and also supported by DOE-NNSA (CDAC) and the NSF grant EAR-2223273 (Synchrotron Earth and Environmental Science, SEES). Work at UAB was supported by NSF CAREER Award No. DMR-2045760.

Author contributions

D.H. conceived the project. E.H.T.P., G.F., R.T., J.-W.K., D.H., R.K., Y.X., D.P. carried out x-ray measurements. E.H.T.P. and Z.L. carried out IR measurements. G.J., S.S., and W.B. carried out transport measurements. Y.W. carried out neutron scattering measurements. N.N. and H.P. carried out DFT+U calculations. M.V. carried out cluster calculations. H.Z., J.F.M. and J.Y. synthesized samples. J.F.M. and H.Z. performed SQUID magnetization measurements. E.H.T.P. carried out data analysis with guidance from D.H., G.F., J.-W.K., Z.L., Y.X., and R.J.H. The manuscript was written by D.H. and E.H.T.P. with input from all authors.

Competing interests

The authors declare no competing interests.

Additional information

Supplementary information The online version contains supplementary material available at https://doi.org/10.1038/s42005-025-02174-2.

Correspondence and requests for materials should be addressed to D. Haskel.

Peer review information *Communications Physics* thanks Atsushi Fujimori and the other, anonymous, reviewer(s) for their contribution to the peer review of this work. A peer review file is available.